

Convolutional LSTM Surrogate for Mesoscale Hydrocode Simulations of Granular Wave Propagation

Kathleen Winona Vian Martinus¹, Sushan Nakarmi¹,
Dawa Seo², Nitin Pandurang Daphalapurkar^{1*}

¹ Theoretical Division

Los Alamos National Laboratory

P.O. Box 1663, Los Alamos, NM 87545

² Civil and Environmental Engineering

Wayne State University, 5050 Anthony Wayne Dr, Detroit, MI 48202

Abstract

Granular materials subjected to impact loading exhibit highly heterogeneous spatiotemporal dynamics governed by wave propagation, pore collapse, and grain-scale rearrangements. Mesoscale hydrocodes resolve these processes but are computationally expensive, limiting their use in parametric studies and uncertainty quantification. In this work, we develop a convolutional Long Short-Term Memory (ConvLSTM) neural network as a spatiotemporal surrogate for mesoscale simulations of weak shock propagation in granular media. Using two-dimensional hydrocode simulations as training data, we first consider a simplified “billiard break” problem in which a cue ball impacts a cluster of nine circular balls, all deformable. Sequences of pressure-field images

Corresponding author: nitin@lanl.gov

serve as input–output pairs for a sequence-to-sequence ConvLSTM, which is trained to predict future frames from a short history. We compare several architectures and show that a relatively compact encoder–decoder ConvLSTM accurately reproduces the propagation of the pressure wave and the resulting particle motion for an unseen combination of cue-ball position and impact velocity. As a proof-of-concept extension, we apply the same ConvLSTM framework to previously published mesoscale simulations of weak shock compaction in a granular ensemble. When evaluated at piston impact speeds that were completely withheld from training, the surrogate captures the position and shape of the compaction front and its dependence on impact speed, while smoothing fine pore-scale details in the highly compacted region as expected. These results demonstrate that ConvLSTM models can serve as satisfactory surrogates for spatiotemporal mesoscale simulations of granular wave propagation, enabling accelerated exploration of parameter space and laying the groundwork for physics-informed, mesoscale simulations of granular materials under shock loading.

Keywords

1 shock wave, impact, dynamic loading, deformation, machine learning

2 1 Introduction

3 Granular materials under dynamic loading arise in a broad spectrum of applications, in-
4 cluding powder metallurgy, mining, deformation of energetic materials, and crater forma-
5 tion [1, 2]. Their response is governed by complex interactions between grains, pores, and
6 propagating stress waves, leading to heterogeneous fields of pressure, strain, and velocity at
7 the mesoscale. Resolving these mechanisms is essential for reliable continuum-scale models,
8 but direct experimentation often lacks the spatial and temporal resolution needed to fully
9 characterize statistically representative pore-scale dynamics [3].

10 Mesoscale numerical simulations, in which individual grains are modeled as deformable solids
11 with explicit pore structures, have emerged as a powerful tool to bridge the gap between
12 grain-scale physics and bulk response [1, 4]. Recent work using Los Alamos National Lab-
13 oratory’s (LANL) Free Lagrange (FLAG) hydrocode has demonstrated the importance of
14 pore-size distribution (PSD), particle shape, and initial contact networks for weak shock com-

15 paction in granular salt [5, 2]. These studies show that shock compaction velocity, wavefront
16 thickness, and internal stress substructure are highly sensitive to particle-scale features and
17 that mesoscale modeling provides pore-scale insights inaccessible to traditional continuum
18 descriptions.

19 However, high-fidelity mesoscale simulations are computationally expensive. Each simulation
20 required resolving on the order of ten thousand grains in 2D and fine temporal resolution over
21 many time steps. Consequently, routine tasks such as parametric sweeps, design optimization,
22 and uncertainty quantification become prohibitive when relying exclusively on direct
23 mesoscale computations. This motivates the search for *surrogate models* that approximate
24 the behavior of the mesoscale solver but are sufficiently fast to evaluate repeatedly.

25 Machine learning (ML) offers a natural framework for such surrogates. Recent reviews
26 have documented the rapid growth of ML methods in granular and geomechanical model-
27 ing [6, 7]. Applications include neural constitutive models, encoder–decoder architectures,
28 graph neural networks (GNNs), neural operator methods, and uncertainty quantification.
29 In granular mechanics, GNN-based surrogate models have been shown to accelerate discrete
30 element method (DEM) simulations of granular flows by orders of magnitude while retaining
31 accuracy [8]. Deep active learning and transfer learning strategies have been used to build
32 data-driven constitutive models from DEM simulations of granular soils [9, 10, 11]. Recurrent
33 architectures such as Long Short-Term Memory (LSTM) and gated recurrent unit (GRU)
34 networks have been applied to learn stress–strain histories and path-dependent responses in
35 granular materials [12, 13, 14].

36 Despite this progress, most existing ML models for granular materials operate on low-
37 dimensional inputs and outputs, such as scalar stress and strain histories or averaged quan-
38 tities. Full-field spatiotemporal modeling of pressure, velocity, and grain configuration re-
39 mains largely unexplored. In particular, there is limited work on learning the co-evolution
40 of spatially heterogeneous pressure fields and grain-scale kinematics directly from mesoscale
41 continuum simulations.

42 In this paper, we develop a spatiotemporal surrogate model for mesoscale granular wave
43 propagation based on a convolutional Long Short-Term Memory (ConvLSTM) neural net-
44 work [15]. ConvLSTM extends the classical LSTM by replacing dense matrix multiplications
45 with convolutions, enabling it to capture spatial correlations in image sequences while main-
46 taining temporal memory. We train the ConvLSTM on sequences of images rendered from
47 FLAG hydrocode simulations, where color encodes the pressure field and grain positions in
48 a two-dimensional domain.

49 We first focus on a simplified “billiard break” problem in which a cue ball impacts a cluster
50 of nine circular balls. This system provides a controlled setting for developing and test-
51 ing the methodology. We vary the cue-ball position and velocity to generate a family of
52 mesoscale trajectories and use them to train and test the ConvLSTM. We then apply the
53 same architecture to mesoscale simulations of weak shock compaction in a granular ensem-
54 ble of circular grains from Seo et al. [5], using piston impact speed as a control parameter.
55 The compaction problem is treated as a proof-of-concept extension to assess whether the
56 ConvLSTM trained on mesoscale data can interpolate across impact speeds and reproduce
57 the large-scale features of the compaction front.

58 The remainder of the paper is organized as follows. Section 2 summarizes related work
59 on ML for granular materials and LSTM-based approaches for path-dependent behavior.
60 Section 3 describes the FLAG hydrocode simulations, the image-based data representation,
61 and the ConvLSTM architecture and training procedure. Section 4 presents results for the
62 billiard problem and the granular compaction extension. Section 5 discusses implications,
63 limitations, and opportunities for future work. Conclusions are given in Section 6.

64 2 Background

65 Recent advances in machine learning have enabled novel modeling approaches for granular
66 materials across scales. A comprehensive review by Wang et al. [6] and the references therein
67 categorizes ML applications at both the grain scale and the bulk continuum scale, including
68 neural constitutive modeling, encoder-decoder networks, graph learning, neural operator
69 methods, and uncertainty quantification. This work identifies growing interest in integrating
70 physical priors and domain knowledge into data-driven methods.

71 Fransen et al. [7] discuss key challenges for applying scientific machine learning to granular
72 simulations, particularly at the continuum scale. Their position paper highlights the im-
73 portance of sequence models, graph-based representations, and probabilistic surrogates for
74 capturing the complex, multiscale nature of granular mechanics.

75 Choi and Kumar [8] demonstrate the potential of graph neural networks (GNNs) to serve as
76 surrogate models for granular flows such as column collapses. Their graph neural simulator
77 (GNS) achieves orders-of-magnitude speedup compared to traditional simulation while main-
78 taining high predictive accuracy. Qu et al. [9] proposed a deep active learning framework
79 for modeling granular material response using Discrete Element Method (DEM) data. In
80 related work, Qu et al. [10] apply knowledge transfer techniques for multiscale modeling, en-
81 abling efficient training from synthetic datasets and improving generalization across loading
82 regimes.

83 Several publications have explored the use of recurrent neural networks (RNNs) and, in par-
84 ticular, Long Short-Term Memory (LSTM) networks for modeling the path-dependent me-
85 chanical response of granular materials. A study on deep transfer learning-aided constitutive
86 modeling [11] trained LSTM models on DEM simulations, capturing complex stress-strain
87 relationships under cyclic and monotonic loads. Zhang et al. [12] demonstrated that both
88 LSTM and GRU networks perform effectively in learning stress-strain behavior from DEM-
89 based triaxial tests. To address history dependence, Ma et al. [13] introduced a modified
90 LSTM architecture in which the initial hidden state encodes the granular material’s physi-
91 cal state (e.g., density, stress), enabling accurate predictions under non-monotonic loading
92 paths. Additional work on LSTM-based surrogates has focused on modeling granular flow
93 fields and their evolution in time [14], showing promising results in replacing time-expensive
94 DEM simulations. Ulloa et al. [16] extend model-free data-driven mechanics to micromor-
95 phic continua, enabling simulations of strain-localizing/softening materials that capture the
96 intrinsic material length scale and associated instabilities without prespecifying a failure
97 mode.

98 Mesoscale simulations for shock compaction of granular materials have advanced significantly.
99 Vogler et al. [1] and others used mesoscale finite element simulations to explore differences
100 between two- and three-dimensional (2D and 3D) formulations and the effects of contact
101 laws on dynamic compaction. More recently, Seo and co-workers conducted systematic
102 mesoscale studies of weak shock compaction in granular salt (square grain morphology),
103 focusing on pore-size distribution (PSD) effects [5] and related configurations [2]. These
104 works showed that the shock compaction velocity and front structure depend strongly on
105 PSD, particle shape, and initial contact configurations, and introduced statistical metrics
106 such as coordination number, mean pore diameter, and bimodality coefficient to characterize
107 PSD.

108 Despite the breadth of these contributions, most prior LSTM/GRU models for granular
109 materials have commonly focused on low-dimensional inputs. The co-evolution of field-
110 level pressure and particle-level positions is a unique, multiphysics ML target that is not
111 handled in existing literature. Likewise, ML modeling of granular materials via continuum
112 solvers, especially with elastodynamic fidelity (e.g., accounting for shocks, reflections, and
113 wave interference), remains largely unexplored. Spatially aware LSTM architectures such
114 as ConvLSTM have not been widely applied to granular material modeling, particularly for
115 continuum-level fields derived from elastodynamic hydrocodes. This work bridges that gap
116 by combining high-fidelity mesoscale simulations with ConvLSTM-based surrogates to learn
117 the spatiotemporal evolution of pressure fields and grain configurations.

118 3 Methods

119 3.1 Mesoscale Modeling using FLAG hydrocode

120 Our prior work developed a mesoscale computational model to simulate the shock compaction
121 test with square-shaped grains using the FLAG [17, 18] hydrodynamic code. The Lagrangian
122 method was preferred because interface tracking is natural to this method, and physically
123 based contact models can be employed. Since impact velocities were in a weak shock regime,
124 we did not anticipate any issues related to mesh distortion. In this work, the simulations
125 employed circular grains within a two-dimensional simulation setting while retaining the
126 mechanical properties of salt grains. Frictional forces, both the friction between grains and
127 the friction between the grain and tube walls, were not accounted for in the model.

128 Discretization involved creating a mesh of a four-node element (aka a zone) within a material
129 domain occupied by a particle. FLAG then solves for field variables and thermodynamic
130 quantities using material constitutive and equation of state continuum models accounting
131 for normal contact between the deformable balls. Mesh convergence studies were performed
132 to select a zone size that resolves stress gradients associated with small-scale features while
133 balancing computational cost [2]. However, using more zones for higher mesh resolution can
134 be computationally expensive. Therefore, it was essential to determine a reasonable mesh
135 resolution that balances the numerical solution's accuracy and efficiency.

136 In this study, we used an elastic-plastic response with linear hardening, along with the

137 equation of state referencing the SESAME (Salt: 7282, Sapphire: 7411, Brass: 4100) ([19]).
 138 Each simulation was performed using high-performance computing at LANL, utilizing 144
 139 processors across four nodes spanning 12 hours. The mesoscale procedure was previously
 140 validated against the measured U_s - U_p response for granular salt, as reported in Seo et al.
 141 (2024)[2]. We applied the same testing setup (see Figure 14 in Ref. [2]) and material
 142 properties in this work as in Seo et al. (2024)[2] (Table 1).

Materials	<u>Salt</u> [20]	<u>Brass</u> [21, 22]	<u>Sapphire</u> [23, 24]
Density (g/cm ³)	single grain: 2.16; sample: 1.41	8.47	3.97
Shear modulus (GPa)	10.48	38.7	175
Hardening modulus (GPa)	2.34	20	20
Yield strength (MPa)	11.8	337	380
SESAME table	7282	4100	7411

Table 1: Material Properties for mesoscale simulations

143 3.2 Mesoscale hydrocode simulations

144 3.2.1 Billiard impact problem

145 We first consider a simplified two-dimensional “billiard break” configuration consisting of
 146 nine circular balls in contact, impacted by a single “cue ball” at varying positions and ve-
 147 locities. All simulations were performed with the FLAG hydrocode, using the same material
 148 model, equation of state, and boundary conditions as in Seo et al. [5]. The billiard problem
 149 is treated as a mesoscale elastodynamic system in which the impacting cue ball generates a
 150 transient stress wave traversing through individual grains, that then propagates through the
 151 particle assembly and induces particle motion.

152 In total, twelve distinct FLAG simulations of the 10-ball billiard configuration were carried
 153 out. Each simulation differed in the *initial position* and *velocity vector* of the cue ball. The
 154 cue ball was initialized at three locations along the lower boundary of the domain,

$$(x_0, y_0) \in \{(0.0, -4.0), (1.0, -4.0), (-1.0, -4.0)\} \text{ cm}, \quad (1)$$

155 and launched with one of four velocity vectors,

$$(v_x, v_y) \in \{(0.003, 0.02), (0.003, 0.03), (0.002, 0.02), (0.002, 0.03)\} \text{ cm}/\mu\text{s}. \quad (2)$$

156 Changing the horizontal and vertical components of the velocity simultaneously varied both
 157 the impact speed and the incident angle of the cue ball, as well as the overall momentum
 158 input into the granular assembly.

159 For the billiard case, the FLAG time integration used a maximum time step of $dt_{\max} =$
 160 $0.025 \mu\text{s}$ and a final time $t_{\text{stop}} = 2000 \mu\text{s}$. Data including pressure and particle positions
 161 were written every 70 time steps and post-processed into two-dimensional color images. This

162 output resulted in 1,152 images per simulation and 13,824 total images between the twelve
163 simulations.

164 Of the twelve simulations, ten were used for training the ConvLSTM model and two were
165 reserved exclusively for testing. The test simulations correspond to

166

- 166 • Test set 1: $(v_x, v_y) = (0.002, 0.03)$ cm/ μ s, cue-ball position $(1.0, -4.0)$ cm,
- 167 • Test set 2: $(v_x, v_y) = (0.002, 0.03)$ cm/ μ s, cue-ball position $(-1.0, -4.0)$ cm.

168 The individual velocities and positions appearing in these test cases are present in the training
169 set, but the specific *combinations* of position and velocity of the cue ball used in the test
170 runs are not. This design probes the model's ability to interpolate between previously seen
171 initial conditions without requiring extrapolation to completely unseen parameter ranges. A
172 validation set was constructed by randomly withholding 10% of the training sequences (at
173 the sequence level), using a validation fraction of 0.1 in the data loader.

174 **3.2.2 Granular compaction problem**

175 As a proof-of-concept extension beyond the simplified billiard system, we also applied the
176 ConvLSTM framework to weak shock compaction of a dense granular medium. These sim-
177 ulations follow the mesoscale setup of Seo et al. [5], in which circular grains represent a
178 granular solid impacted by a rigid piston. The material model (SESAME equation of state
179 for NaCl and elastic-plastic constitutive response with linear hardening), boundary condi-
180 tions (rigid piston, lateral confinement, and particle–wall interactions), and overall numerical
181 settings are identical to those used in that prior work.

182 In the full granular compaction simulations, the total number of finite volume zones (equiv-
183 alent to finite elements) in the domain is on the order of several thousand. For training
184 the ConvLSTM surrogate, we extracted a focused sub-window of the domain containing
185 several hundred grains (fewer than one thousand) near the compaction front. This cropped
186 region captures the evolving shock front, particle rearrangements, and porosity evolution
187 while keeping the image resolution compatible with the ConvLSTM input size.

188 We ran ten granular compaction simulations with eight used for training the ConvLSTM
189 model and two reserved exclusively for testing. A validation set was constructed by randomly
190 withholding 10% of the training sequences at the sequence level.

191 The only parameter varied across simulations was the piston impact speed, which was sam-
192 pled between 50 m/s and 400 m/s. All simulations with piston speeds in this range, excluding
193 100 m/s and 300 m/s, were used for training the ConvLSTM. The simulations at 100 m/s and
194 300 m/s were completely withheld from training and served as independent test cases to as-
195 sess the surrogate's ability to interpolate across impact speeds in a more complex granular
196 setting. We use the following impact velocities in our simulations:

$$v \in \{50, 100, 150, 200, 250, 275, 300, 350, 375, 400\} \times 10^{-4} \text{ cm}/\mu\text{s}. \quad (3)$$

197 FLAG simulations were advanced with a maximum time step of $dt_{\max} = 0.001 \mu\text{s}$ and
198 terminated at a final time of $15 \mu\text{s}$. Output was written at fixed physical-time intervals
199 of $0.01 \mu\text{s}$ and post-processed into two-dimensional color images. This time-based output
200 produced in 1,501 images per simulation, for a total of 15,010 images across the ten granular
201 compaction simulations.

202 3.3 Image representation and sequence construction

203 The surrogate is trained to learn the rendered field rather than raw pressure values. For
204 both the billiard and granular compaction problems, FLAG field outputs were converted
205 into two-dimensional color images. Each saved frame was written to disk as a 128×128
206 RGB image, where color encodes both the pressure field and the configuration of particles.
207 The exact mapping of RGB values, encoding both pressure and geometric information, is
208 determined by the visualization pipeline implemented in the open-source ParaView software
209 package.

210 Images were loaded using TensorFlow’s utility, which returns tensors of shape $(128, 128, 3)$
211 with integer pixel intensities in the range $[0, 255]$. For each image, we convert the RGB values
212 to floating point and normalize each channel by dividing by 255, resulting in pixel values
213 scaled to the range $[0, 1]$. Because the particle shapes, positions, and pressure magnitudes
214 are all encoded in the RGB color values, no additional binary masks or explicit particle labels
215 are required; the spatial structure of the granular assembly is implicitly represented in the
216 color image.

217 We adopt a sequence-based, sliding-window formulation that enables the ConvLSTM model
218 to learn temporal dependencies across image frames. We define overlapping input sequences
219 of ten consecutive frames,

$$\mathbf{x}_t = [f_t, f_{t+1}, \dots, f_{t+9}], \quad (4)$$

220 which are extracted from each simulation and mapped to corresponding target sequences

$$\mathbf{y}_t = [f_{t+1}, f_{t+2}, \dots, f_{t+10}], \quad (5)$$

221 where f_t denotes the image at frame index t . During training, these sequences are incremen-
222 tally shifted forward in time, allowing temporal overlap between samples and increasing the
223 effective size of the training set. The model is optimized to predict multiple future frames
224 from each input sequence, with the loss evaluated only on the terminal prediction. This pro-
225 motes stable learning of multi-step temporal dynamics and avoids the instability associated
226 with fully autoregressive rollouts.

227 During inference, the trained model is initialized using only the first ten frames and applied
228 iteratively in a sliding-window manner. Each prediction step produces a 10-frame sequence
229 of future timesteps, and only the terminal frame from that sequence is retained and used
230 to construct the next input window. As a result, feedback occurs at the level of multi-step
231 evolution rather than through direct one-step recursion, which reduces error accumulation
232 and promotes more stable long-horizon predictions.

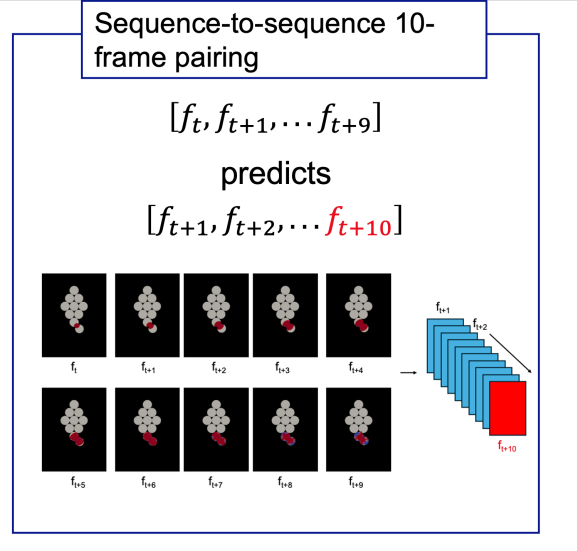


Figure 1: Sliding window approach during training

233 We note that while neural-operator methods are a powerful alternative for learning parametric
 234 solution maps of PDEs, they are most naturally applied to problems with clearly defined
 235 field variables on consistent discretizations and with ample coverage of the parameter space.
 236 In contrast, our training data consist of rendered RGB frames that jointly encode pressure
 237 and evolving particle geometry (interfaces, contacts, and topology changes) in a strongly
 238 transient, weak-shock regime. Given the limited number of expensive mesoscale trajectories
 239 available for training and the presence of sharp moving wavefronts and contact-driven dis-
 240 continuities, we adopt a ConvLSTM architecture as a pragmatic and robust image-sequence
 241 surrogate. ConvLSTM directly models spatiotemporal correlations in the rendered fields
 242 without requiring explicit interface tracking or operator inputs, and provides stable multi-
 243 step predictions under our sliding-window training strategy. Neural operators remain a
 244 promising direction for future work, particularly as larger parametric datasets and explicit
 245 field representations become available.

246 3.4 Convolutional LSTM architecture

247 We adopt an encoder-decoder ConvLSTM architecture that captures both local spatial struc-
 248 ture and temporal evolution in the image sequences. ConvLSTM replaces the fully connected
 249 operations in a standard LSTM with convolutions, enabling the network to maintain spatially
 250 structured hidden states [15]. In each ConvLSTM layer, the input-to-state and state-to-state
 251 transitions are implemented as convolutions, and the gating mechanisms (input, forget, and
 252 output gates) operate on feature maps rather than vectors.

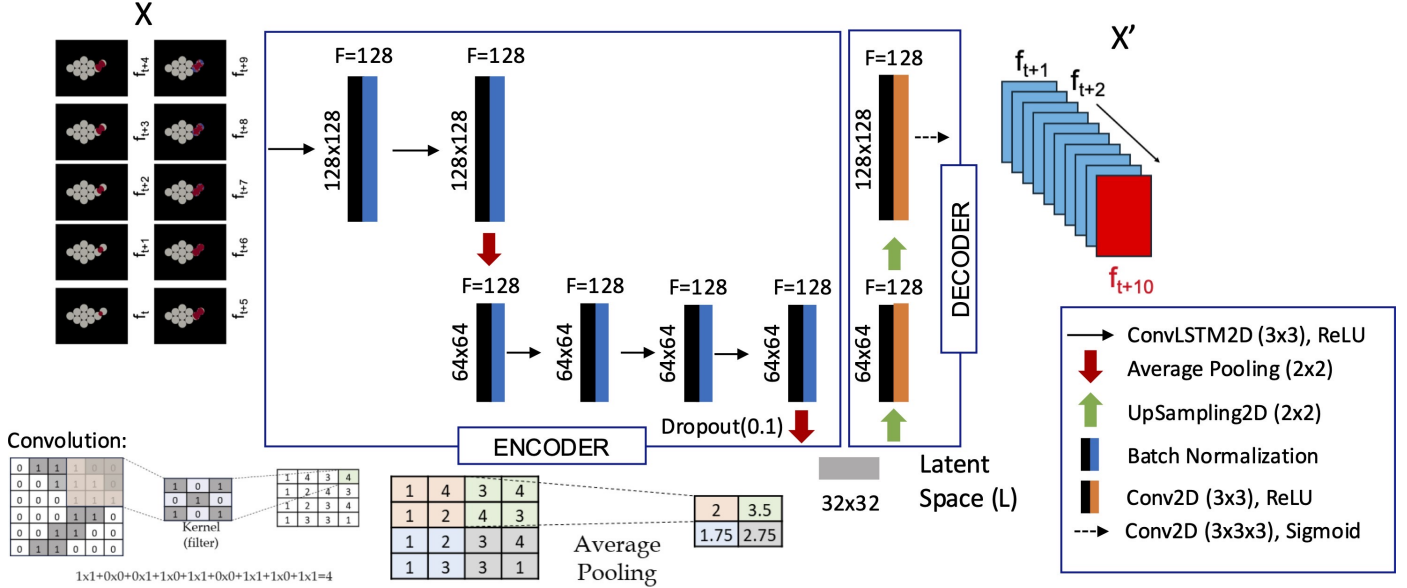


Figure 2: Schematic of the encoder-decoder ConvLSTM architecture used in this work, showing ConvLSTM layers, pooling/upsampling operations, and the sequence-to-sequence mapping from input frames to predicted frames.

253 The encoder consists of a stack of ConvLSTM layers with increasing receptive field, inter-
 254 leaved with spatial downsampling. In the configuration used here, six ConvLSTM layers are
 255 applied in sequence, each with 128 filters and 3×3 kernels and rectified linear unit (ReLU)
 256 activations. After the second and fourth ConvLSTM layers, we apply average pooling to
 257 reduce the spatial resolution, yielding a latent representation on a 32×32 grid. This grad-
 258 ual reduction in spatial resolution allows the network to aggregate information over larger
 259 spatial neighborhoods while controlling the number of parameters.

260 The decoder mirrors the encoder structure and reconstructs the full-resolution image se-
 261 quence from the latent representation. It consists of two ConvLSTM layers with 128 filters
 262 and ReLU activations, followed by upsampling operations that restore the spatial resolution
 263 to 128×128 , matching the input size. A final ConvLSTM layer with a sigmoid activation
 264 produces the output sequence, with three channels corresponding to the RGB intensities at
 265 each pixel.

266 We explored several architectural variants, including different numbers of layers, kernel sizes
 267 (3×3 vs. 5×5), numbers of filters per layer, and pooling strategies Table 2. These vari-
 268 ants were compared using mean squared error (MSE) and mean structural similarity index
 269 (MSSIM) on held-out billiard test simulations, as well as training time and parameter count.
 270 While deeper models with more filters offer slightly improved SSIM in some cases, we find
 271 that a relatively compact architecture with 3×3 kernels and two pooling stages provides a
 272 favorable balance between accuracy and computational cost. The final architecture described
 273 above is used for all results reported in this work.

274 **3.5 Training and evaluation metrics**

275 The ConvLSTM networks are trained using a mean squared error (MSE) loss between pre-
276 dicted and ground-truth images. Although the model predicts multiple future frames for
277 each input sequence, the loss is evaluated only on the terminal predicted frame. For this
278 frame, the squared difference between predicted and true RGB intensities is computed for
279 each pixel and channel and averaged to yield a scalar loss. Optimization is performed using
280 the Adam optimizer with minibatches of sequence pairs $(\mathbf{x}_t, \mathbf{y}_t)$ drawn from the training set.

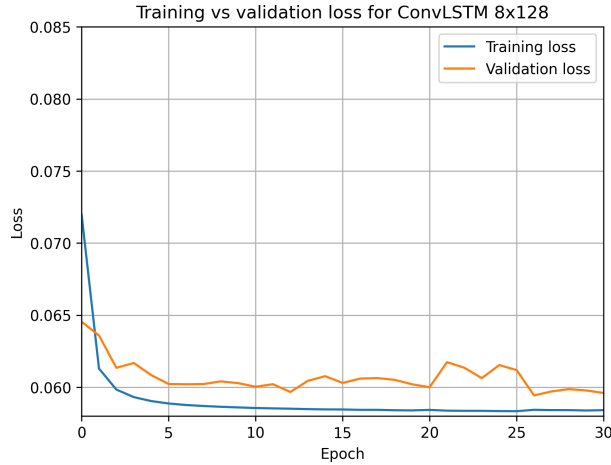


Figure 3: Training and validation loss for ConvLSTM 8x128 (3x3) model

281 Figure 3 shows the evolution of the training and validation loss over epochs. Both curves
282 decrease monotonically and plateau after 30 epochs. Convergence of validation loss suggests
283 no obvious overfitting of the ConvLSTM model.

284 To assess perceptual similarity between predicted and reference images, we compute the
285 structural similarity index (SSIM) on a per-frame basis. For a given frame index k , we
286 compare the predicted image \hat{f}_k to the corresponding FLAG image f_k and evaluate SSIM
287 over all pixels and channels, yielding a scalar value in $[-1, 1]$ (with 1 indicating perfect
288 agreement). In the figures, we report SSIM as a function of frame index for each test case,
289 and in the tables we quote representative values or averages over selected time intervals.
290 In both the billiard and granular compaction problems, SSIM provides a more informative
291 measure of visual and structural agreement than MSE alone, as it accounts for local contrast
292 and texture as well as overall intensity.

293 To identify the best ConvLSTM architecture, we conducted hyperparameter tuning by vary-
294 ing filter sizes, amount of filters, kernel sizes, and amount of average pooling. Six different
295 ConvLSTM frameworks were trained on the FLAG dataset, evaluated on Mean Squared
296 Error (MSE) and Structural Similarity Index (SSIM) [25].

297 SSIM is a method of comparing how similar two images are to each other by evaluating
298 structural information losses. As opposed to error-sensitivity methods such as MSE, which
299 purely calculate differences in pixel values between images, SSIM focuses on capturing per-

300 perceptual quality measures of an image. In this way, SSIM evaluates differences in images
 301 with the goal of approximating how the human visual system (HVS) perceives structural
 302 differences.

303 SSIM is recorded on a scale from -1 to 1 , where 1 indicates that the images are exactly
 304 similar, and values near zero or negative indicate large differences between the images. SSIM
 305 considers three characteristics of an image in its comparison: *luminance*, *contrast*, and *struc-
 306 ture*.

307 Specifically, let x and y be two corresponding regions of two different images extracted from
 308 the same spatial location. Luminance l , contrast c , and structure s are defined as:

$$l(x, y) = \frac{2\mu_x\mu_y}{\mu_x^2 + \mu_y^2}, \quad c(x, y) = \frac{2\sigma_x\sigma_y}{\sigma_x^2 + \sigma_y^2}, \quad s(x, y) = \frac{\sigma_{xy}}{\sigma_x\sigma_y},$$

309 where μ_x , μ_y , σ_x^2 , σ_y^2 , and σ_{xy} denote the mean of x , the mean of y , the variance of x , the
 310 variance of y , and the covariance between x and y , respectively.

311 A basic similarity index can then be defined as the product of these three components:

$$S(x, y) = l(x, y) c(x, y) s(x, y) = \frac{4\mu_x\mu_y\sigma_{xy}}{(\mu_x^2 + \mu_y^2)(\sigma_x^2 + \sigma_y^2)}.$$

312 However, this expression becomes unstable when the denominator approaches zero. To
 313 address this, the final SSIM index introduces stabilizing constants:

$$SSIM(x, y) = \frac{(2\mu_x\mu_y + C_1)(2\sigma_{xy} + C_2)}{(\mu_x^2 + \mu_y^2 + C_1)(\sigma_x^2 + \sigma_y^2 + C_2)}.$$

314 The constants C_1 and C_2 are defined as:

$$C_1 = (K_1 L)^2, \quad C_2 = (K_2 L)^2,$$

315 where L is the dynamic range of pixel values in the image ($L = 1$ for normalized RGB
 316 images, $L = 255$ for standard grayscale images), and K_1 and K_2 are small constants chosen
 317 such that C_1 and C_2 only influence the computation when the denominator is close to zero.

318 Table 1 below shows the MSE and MSSIM values of the six frameworks, evaluated using
 319 two FLAG test data sets that the ML framework did not see during training. The lowest
 320 MSE and highest MSSIM for each data set are highlighted in red, with the chosen framework
 321 in bold. The framework in bold was chosen as it balanced a high MSSIM value across the
 322 two data sets with training time (the framework with the highest MSSIM values had nearly
 323 double the training time despite similar MSSIM).

Model	# params	MSE (D1)	MSSIM (D1)	MSE (D2)	MSSIM (D2)	Train (s)
ConvLSTM (3x3): 8x64, 4xAvgPool	2,375,747	0.006355	0.958071	0.006226	0.952963	5367.73
ConvLSTM (3x3): 4x64-4x128, 4xAvgPool	5,536,163	0.005914	0.94914	0.005750	0.94468	5371.04
ConvLSTM (3x3): 8x128, 2xAvgPool	8,936,611	0.007791	0.98812	0.007676	0.98269	6456.06
ConvLSTM (5x5): 4x64-4x128, 2xAvgPool	15,371,875	0.0077907	0.988212	0.0076802	0.982773	12402.13
ConvLSTM (5x5): 8x64, 1xAvgPool	6,601,155	0.0077497	0.98685	0.007640	0.981050	5703.95
ConvLSTM (5x5): 8x128, 1xAvgPool	26,309,507	0.005812	0.91837	0.0058123	0.9097877	6468.81

Table 2: Comparison of ConvLSTM architectures on the billiard problem. For each model, we report the number of trainable parameters, mean squared error (MSE) and mean SSIM (MSSIM) on two billiard test simulations, and training time.

324 The layers of the encoder process the input sequence both spatially and temporally, allowing
 325 the network to extract hierarchical spatiotemporal features. Spatial resolution is progres-
 326 sively reduced through average pooling operations applied after the second and fourth Con-
 327 vLSTM layers. These pooling steps downsample the feature maps from the initial resolution
 328 of 128x128 to 64x64, and subsequently to 32x32 pixels, thereby compressing the spatial
 329 information while preserving temporal dependencies. The output of the final encoder layer
 330 forms a latent representation of the input sequence at a spatial resolution of 32x32 and a
 331 temporal depth of 10 steps.

332 The decoder consists of two ConvLSTM layers, each also configured with 128 filters and ReLU
 333 activations. To reconstruct the original spatial resolution, we apply upsampling operations
 334 after each decoder layer. Specifically, the spatial dimensions are upsampled from 32x32 to
 335 64x64 after the first decoder layer, and from 64x64 to 128x128 after the second, restoring
 336 the resolution to match the input size. The final output layer is a ConvLSTM layer with a
 337 sigmoid activation function, which produces the predicted frame sequence with pixel values
 338 normalized between 0 and 1.

339 This architecture is well-suited for modeling complex pressure propagation patterns captured
 340 in the training set. The ConvLSTM layers capture these dynamics by maintaining memory
 341 over time while convolving over spatial neighborhoods, allowing the model to learn how
 342 localized pressure changes propagate through space. The hierarchical structure of the encoder
 343 extracts features at multiple spatial resolutions, enabling the network to capture both fine-
 344 grained details and broader propagation patterns. The decoder then reconstructs these
 345 learned spatiotemporal representations into full-resolution predictions, effectively modeling
 346 the pressure field’s evolution over time. As a result, the network can satisfactorily forecast
 347 pressure propagation in this billiards ball example.

348 As summarized schematically in Figure 2, the encoder-decoder ConvLSTM consists of six
349 encoding layers and two decoding layers with intermediate pooling and upsampling.

350 4 Results

351 4.1 Billiard impact surrogate modeling

352 We first evaluate the ConvLSTM surrogate on the 10-ball billiard impact problem. The
353 network is trained on ten FLAG simulations with varying cue-ball positions and velocities,
354 as described in Section 3. Two additional simulations, corresponding to unseen combinations
355 of position and velocity, are reserved as test cases.

356 Figure 4 plots SSIM as a function of frame index for several candidate architectures evaluated
357 on the first billiard test set. SSIM is computed for each frame by comparing the ML predicted
358 image to the corresponding FLAG image and averaging over all pixels. The curves show
359 that the chosen architecture maintains relatively high SSIM over the prediction horizon and
360 compares favorably to deeper and wider alternatives, while requiring fewer parameters and
361 shorter training times.

362 Qualitative comparisons of predicted and reference images are shown in Figure 5. We display
363 selected frames spanning the early, intermediate, and late stages of wave propagation. In the
364 early frames, the ConvLSTM accurately reproduces the initial impact of the cue ball and
365 the emergence of a localized high-pressure region at the contact. As the wave propagates
366 through the finite-volume mesh within each ball, the surrogate captures the primary features
367 of the pressure field, including the wavefront’s shape, position, and interactions with curved
368 boundaries. The predicted ball positions closely track the FLAG simulations, demonstrating
369 that the ConvLSTM has learned the coupling between wave propagation and grain motion
370 encoded in the training data.

371 At later times, as the pressure wave reflects from boundaries and the system approaches a
372 more complex, multi-wave state, minor discrepancies appear in the fine details of the pressure
373 field. However, the global structure of the wave pattern and the overall grain configuration
374 remain well reproduced. Quantitatively, MSE values remain small and SSIM values remain
375 high across both billiard test sets, indicating robust performance under variations of initial
376 cue-ball position and impact velocity.

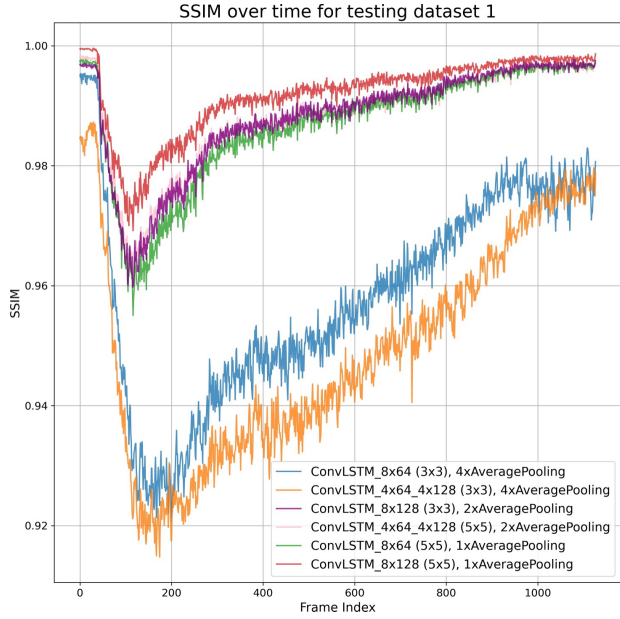


Figure 4: Structural similarity index (SSIM) versus frame index for several ConvLSTM architectures on the first billiard test set. The chosen architecture maintains high SSIM over the prediction horizon while using a moderate number of parameters.

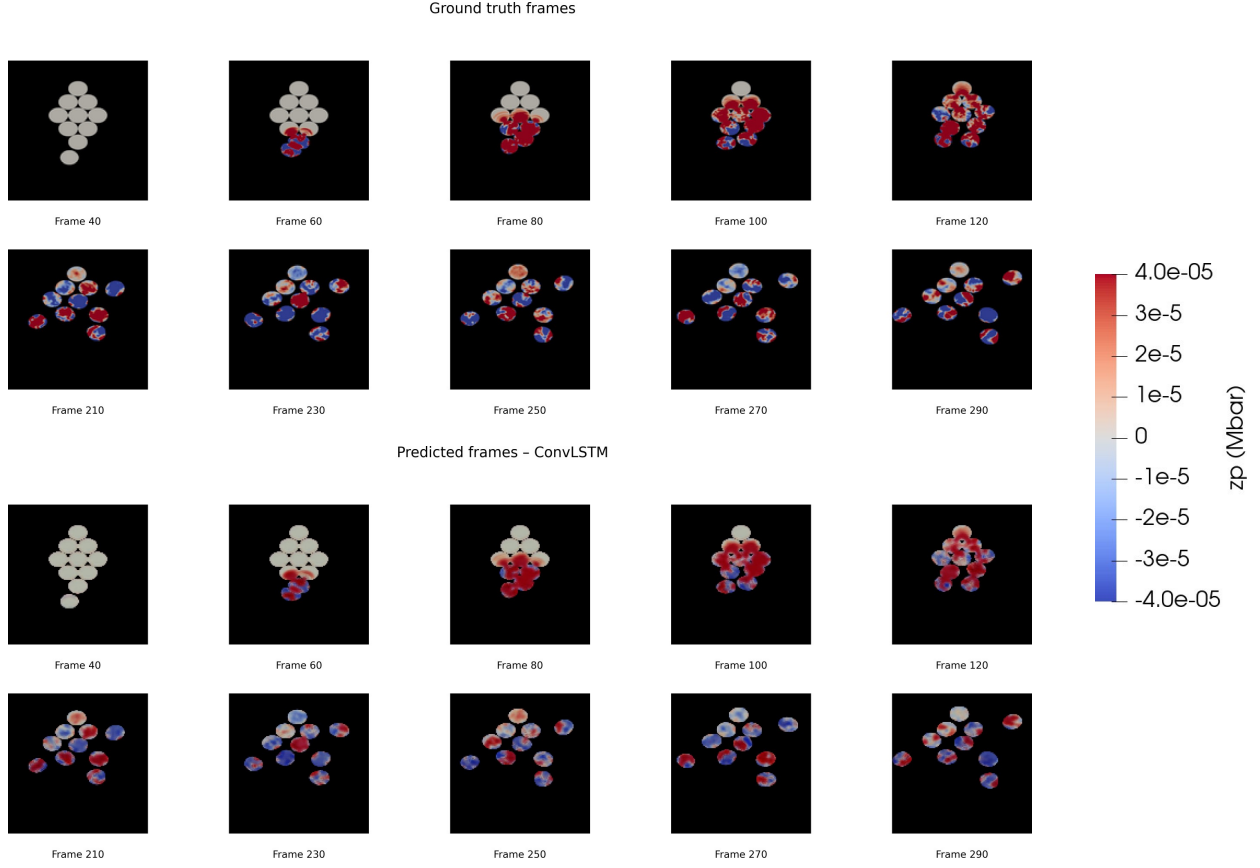


Figure 5: Comparison of ground truth (top) and ConvLSTM predictions (bottom).

377 4.2 Granular compaction: proof-of-concept extension

378 To assess whether the ConvLSTM framework can extend to more realistic granular configura-
 379 tions, we apply the same architecture to mesoscale simulations of weak shock compaction
 380 in granular salt modeled as an ensemble of circular grains. The ConvLSTM framework is
 381 trained in the same manner as for the billiard problem, using sequences of ten frames as
 382 input and predicting the subsequent ten frames. We then evaluate the trained model on the
 383 100 m/s and 300 m/s test case simulations.

384 Qualitative comparisons for the 100 m/s and 300 m/s cases are shown in Figures 6 and 7,
 385 respectively. In both cases, the ConvLSTM successfully captures the *location* and *overall*
 386 *shape* of the compaction front and the primary direction of stress propagation. The predicted
 387 compaction front tracks the FLAG front as it advances into the granular pack, and the broad
 388 structure of the high-pressure region behind the front is reproduced.

389 The surrogate reproduces the front position and large-scale pressure morphology, but attenu-
 390 ates high-frequency pore-scale features in the compacted region—an expected behavior for
 391 convolutional sequence models trained with a pixelwise MSE objective. Once the shock has
 392 traversed a region and the grains have largely collapsed into a dense pack, the high-pressure
 393 zone appears as a more uniform band in the ConvLSTM predictions, with individual grain

394 shapes and small pores no longer resolved as sharply as in the FLAG images. This loss
 395 of sharpness is observed for both 100 m/s and 300 m/s impacts, and is consistent with the
 396 smoothing effect expected from convolutional filters trained with an MSE loss.

397 The SSIM curves in Figure 8 highlight this behavior for the 100 m/s and 300 m/s test cases.
 398 For the 100 m/s case, SSIM tends to decrease over time, indicating that prediction quality
 399 gradually deteriorates as the front advances and the internal stress pattern becomes more
 400 complex. In contrast, for the 300 m/s case, SSIM initially decreases but later recovers and
 401 increases as the simulation proceeds. We interpret this as a consequence of the more uniform
 402 shock front at higher impact speeds: once the front has formed and the compaction pattern
 403 stabilizes, the pressure field becomes easier for the ConvLSTM to predict, leading to higher
 404 structural similarity. Quantitatively, the aggregated MSE and MSSIM values in Table 3
 405 remain on the order of 10^{-3} and around 0.8, respectively, for both test cases.

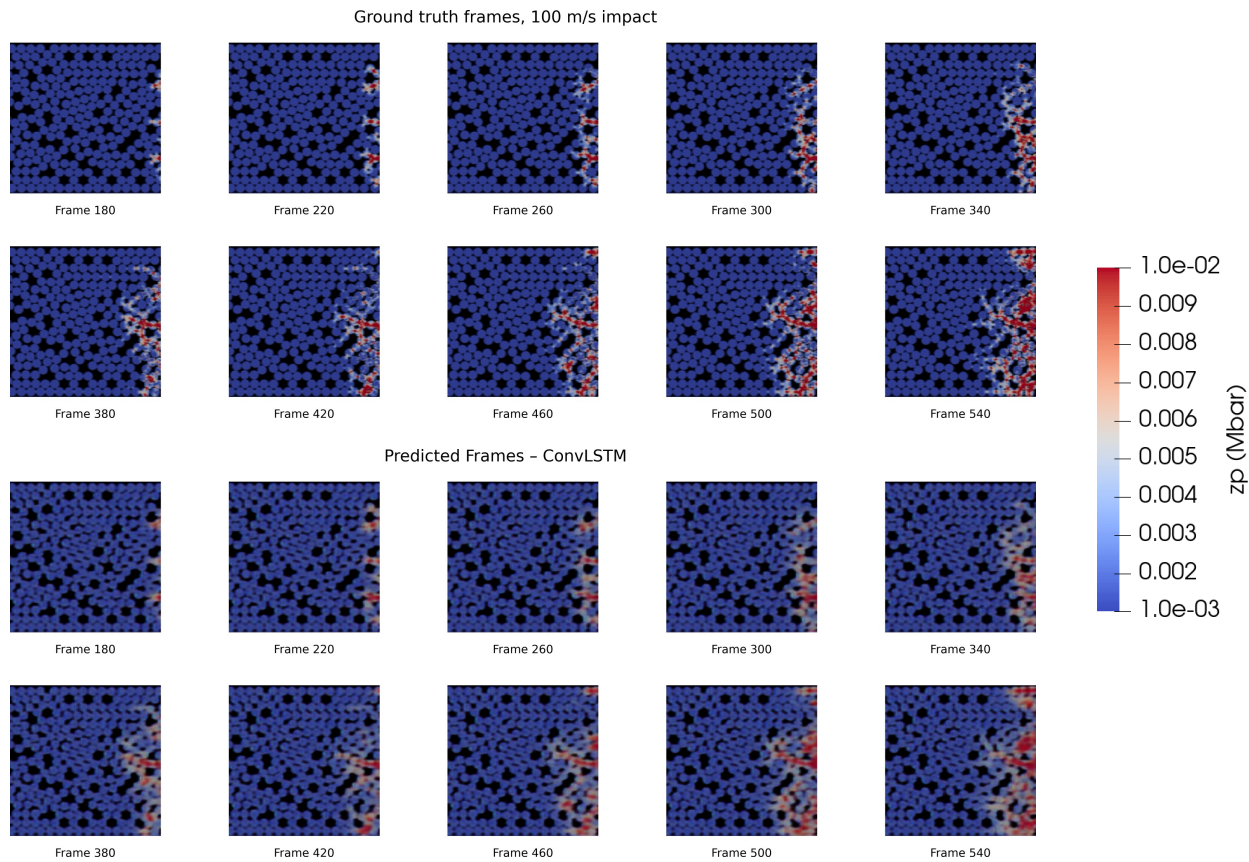


Figure 6: Comparison of FLAG (top) and ConvLSTM (bottom) pressure fields for the granular compaction test at 100 m/s, at selected frames. The ConvLSTM captures the position and overall shape of the compaction front but smooths fine pore-scale details behind the front.

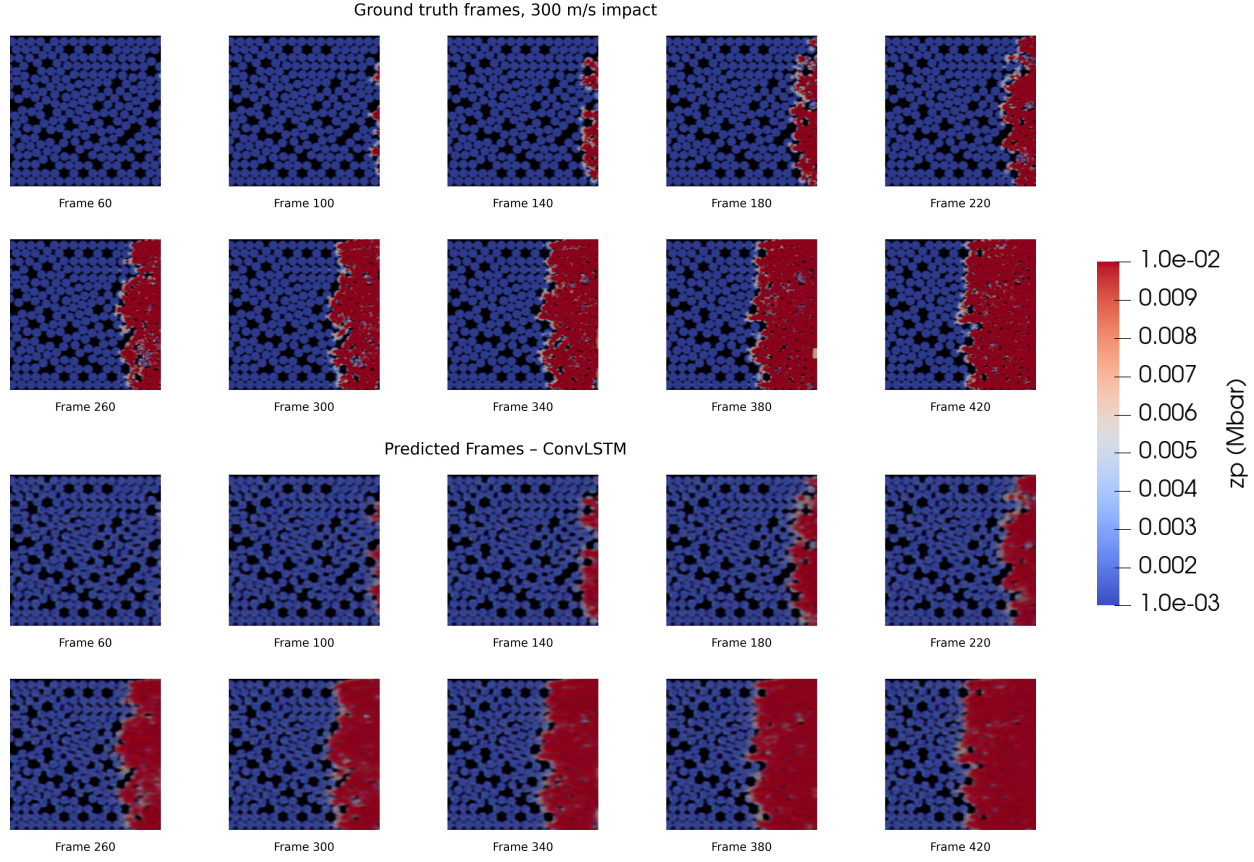


Figure 7: Comparison of FLAG (top) and ConvLSTM (bottom) pressure fields for the granular compaction test at 300 m/s. At higher impact speed the shock front is more uniform, which the ConvLSTM predicts more consistently, while still smoothing small pores in the compacted region.

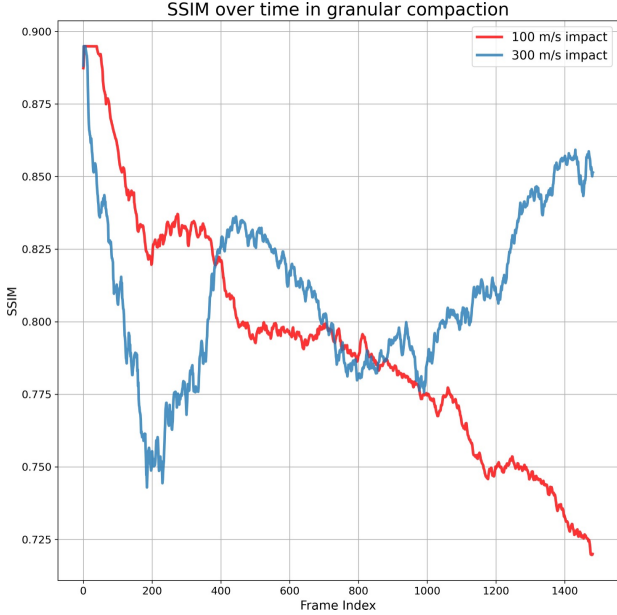


Figure 8: SSIM versus frame index for the granular compaction tests at 100 m/s and 300 m/s. SSIM decreases over time for 100 m/s, whereas for 300 m/s it initially decreases and then recovers as the compaction front becomes more uniform.

Table 3: Mean squared error (MSE) and mean SSIM (MSSIM) for the granular compaction tests at 100 m/s and 300 m/s, averaged over the prediction horizon.

Impact speed	MSE	MSSIM
100 m/s	0.00745	0.793
300 m/s	0.00467	0.810

406 5 Discussion

407 The results presented above demonstrate that ConvLSTM networks trained on mesoscale
 408 hydrocode simulations can serve as effective surrogates for spatiotemporal wave propagation
 409 in granular systems. In the simplified billiard problem, the surrogate accurately predicts the
 410 evolution of both the pressure field and grain positions for unseen combinations of cue-ball
 411 position and velocity. This indicates that the network has learned a representation of the
 412 underlying dynamics that generalizes across initial conditions within the training envelope.

413 The granular compaction problem presents a more stringent test, with thousands of in-
 414 teracting grains, evolving pore structures, and a propagating compaction front. Here, the
 415 ConvLSTM is able to capture the large-scale structure of the shock front and its depen-
 416 dence on impact speed, even when evaluated at piston speeds that were completely withheld
 417 from training. At the same time, the model struggles to reproduce fine pore-scale details
 418 behind the front, particularly in highly compacted regions where grain shapes and small

419 pores are strongly distorted. This limitation is not surprising: the training objective penal-
420 izes pixel-wise errors uniformly, and the convolutional architecture naturally favors smooth
421 approximations of high-frequency structures.

422 From a modeling perspective, these findings highlight both the promise and the current lim-
423 itations of purely data-driven spatiotemporal surrogates for granular mesoscale simulations.
424 On the positive side, ConvLSTM models can be trained to emulate complex, nonlinear dy-
425 namics directly from image sequences, without requiring explicit hand-crafted features or
426 reduced-order representations.

427 On the other hand, the loss of fine-scale resolution suggests several avenues for improvement.
428 First, the training objective could be augmented with multi-scale or perceptual losses that
429 place greater weight on small-scale structures, or with physics-inspired regularization terms
430 that penalize unphysical artifacts. Second, hybrid architectures that combine ConvLSTM
431 layers with attention mechanisms or graph-based representations may offer improved capacity
432 for capturing localized interactions between grains. Third, explicit multi-resolution training
433 strategies could be employed, in which the network is trained to predict both coarse and
434 fine-scale components of the pressure and configuration fields.

435 It is also important to emphasize that, in this work, we deliberately leverage existing, val-
436 idicated mesoscale simulations from Seo et al. [5] as the source of training data. This allows
437 us to focus on the ML methodology and its ability to reproduce known mesoscale behavior,
438 rather than re-establishing the validity of the underlying physics model. A single ConvLSTM
439 rollout of N frames takes $O(1)$ seconds on a GPU vs 12 hours of FLAG CPU time. Future
440 work could combine the ConvLSTM surrogate with experimental data, for example by train-
441 ing on or calibrating to in situ imaging of rapid compaction [26], thereby enhancing fidelity
442 and extending the surrogate beyond the parameter space covered by current simulations.

443 6 Conclusions

444 We have presented a ConvLSTM-based spatiotemporal surrogate model for mesoscale sim-
445 ulations of wave propagation in granular materials. Using high-fidelity FLAG hydrocode
446 simulations as training data, we demonstrated that in a simplified 10-ball billiard impact
447 problem, the ConvLSTM accurately predicts the evolution of pressure fields and grain posi-
448 tions for unseen combinations of initial cue-ball position and velocity. The same ConvLSTM
449 architecture can be applied, without modification, to mesoscale simulations of weak shock
450 compaction in granular salt modeled as an ensemble of circular grains, capturing the position
451 and shape of the compaction front and its dependence on impact speed. The surrogate re-
452 produces large-scale features of the pressure field and compaction front, but tends to smooth
453 fine pore-scale details behind the front, especially in highly compacted regions. These re-
454 sults suggest that ConvLSTM networks provide a promising framework for constructing fast,
455 image-based surrogates of mesoscale hydrocode simulations in granular mechanics. While
456 the current implementation is purely data-driven and uses a simple MSE loss, future work
457 may incorporate physics-informed constraints, multi-scale loss functions, or hybrid architec-
458 tures to improve fidelity at small scales. Such developments would enable more accurate

459 and efficient exploration of parameter space, uncertainty quantification, and coupling to
460 continuum-scale models in applications involving rapid compaction and shock loading of
461 granular materials.

462 Credit authorship contribution statement

463 **Kathleen Martinus:** Conceptualization; Software; Methodology; Formal analysis; Validation;
464 Visualization; Writing – original draft; Writing – reviewing & editing; Data curation.
465 **Dawa Seo:** Software; Methodology; Formal analysis; Validation; Visualization; Writing –
466 reviewing & editing; **Sushan Nakarmi:** Conceptualization; Supervision; Methodology; Val-
467 idation; Writing – original draft; Writing – reviewing & editing. **Nitin Daphalapurkar:**
468 Conceptualization; Supervision; Methodology; Validation; Writing – original draft; Writing
469 – reviewing & editing; Funding acquisition.

470 7 Acknowledgments

471 Research on computational modeling was supported by U.S. Department of Energy’s ASC/PEM/EM
472 through LANL with Christina Scovel as the project leader and D.J. Luscher as the program
473 manager. LANL is operated by Triad National Security, LLC, for the National Nuclear Se-
474 curity Administration of U.S. Department of Energy (Contract No. 89233218CNA000001).

475 Data availability

476 The data supporting the findings of this study are available from the lead author upon rea-
477 sonable request and in accordance with the policies of the Los Alamos National Laboratory.

478 Declaration of generative AI and AI-assisted technolo- 479 gies in the manuscript preparation process

480 During the preparation of this work the authors used OpenAI’s software package chatGPT
481 in order to reason. After using this tool, the authors reviewed and edited the content as
482 needed and take full responsibility for the content of the published article.

483 **References**

484 [1] T. J. Vogler, Rapid compaction of granular material: characterizing two- and three-
485 dimensional mesoscale simulations, *Shock Waves* 23 (2013) 39–52.

486 [2] D. Seo, E. M. Heatwole, T. A. Feagin, I. D. Lopez-Pulliam, D. J. Luscher, A. Koskelo,
487 M. Kenamond, C. Rousculp, C. Ticknor, C. Scovel, et al., Weak shock compaction on
488 granular salt, *Scientific Reports* 14 (1) (2024) 16695.

489 [3] N. D. Parab, B. Claus, M. C. Hudspeth, J. T. Black, A. Mondal, J. Sun, K. Fezzaa,
490 X. Xiao, S. Luo, W. Chen, Experimental assessment of fracture of individual sand par-
491 ticles at different loading rates, *International Journal of Impact Engineering* 68 (2014)
492 8–14. [doi:
493 URL <https://www.sciencedirect.com/science/article/pii/S0734743X14000165>](https://doi.org/10.1016/j.ijimpeng.2014.01.003)

494 [4] X. F. Zhang, L. Qiao, A. S. Shi, J. Zhang, Y. G. Zhang, Mesoscale simulation on the
495 shock compression behaviour of al–w–binder granular composite, *Materials & Design*
496 52 (2013) 391–404.

497 [5] D. Seo, D. J. Luscher, C. A. Scovel, N. P. Daphalapurkar, Mesoscale simulation of
498 granular materials under weak shock compaction–pore size distribution effects, *Journal*
499 *of Applied Physics* 136 (15) (2024) 155902. [doi:
500](https://doi.org/10.1063/5.0229975)

500 [6] M. Wang, K. Kumar, Y. T. Feng, T. Qu, M. Wang, Machine learning aided modeling
501 of granular materials: A review, *Archives of Computational Methods in Engineering* 32
502 (2025) 1997–2034, published online 29 Oct 2024. [doi:
503 URL <https://link.springer.com/article/10.1007/s11831-024-10199-z>](https://doi.org/10.1007/s11831-024-10199-z)

504 [7] S. Fransen, et al., Towards scientific machine learning for granular material
505 simulations—challenges and opportunities, *arXiv preprint arXiv:2504.08766* (2025).

506 [8] Y. Choi, K. Kumar, Graph neural network-based surrogate model for granular flows,
507 *arXiv preprint arXiv:2305.05218* (2023).

508 [9] T. Qu, S. Guan, Y. T. Feng, G. Ma, W. Zhou, J. Zhao, Deep active learning for
509 constitutive modelling of granular materials: From representative volume elements to
510 implicit finite element modelling, *International Journal of Plasticity* 164 (2023) 103576.
511 [doi:
512 URL <https://www.sciencedirect.com/science/article/pii/S0749641923000621>](https://doi.org/10.1016/j.ijplas.2023.103576)

513 [10] T. Qu, J. Zhao, S. Guan, Y. Feng, Data-driven multiscale modelling of granular mate-
514 rials via knowledge transfer and sharing, *International Journal of Plasticity* 171 (2023)
515 103786. [doi:
516 URL <https://www.sciencedirect.com/science/article/pii/S074964192300270X>](https://doi.org/10.1016/j.ijplas.2023.103786)

517 [11] Y. Qu, et al., Deep transfer learning-aided constitutive modelling of granular soils,
518 *Computers and Geotechnics* (2023).

519 [12] Y. Zhang, et al., Deep learning predicts stress-strain relations of granular materials
520 under complex loading, Computer Modeling in Engineering & Sciences 128 (1) (2021)
521 329–350.

522 [13] G. Ma, et al., A predictive deep learning framework for path-dependent mechanical
523 behavior of granular materials, Acta Geotechnica 17 (4) (2022) 1111–1126.

524 [14] L. Lu, et al., Machine learning accelerated discrete element modeling of granular flows,
525 Chemical Engineering Science 246 (2021) 116999.

526 [15] X. Shi, et al., Convolutional LSTM network: A machine learning approach for precipi-
527 tation nowcasting, in: Advances in Neural Information Processing Systems (NeurIPS),
528 Vol. 28, 2015.

529 [16] J. Ulloa, L. Stainier, M. Ortiz, J. E. Andrade, Data-driven micromorphic mechanics
530 for materials with strain localization, Computer Methods in Applied Mechanics and
531 Engineering 429 (2024) 117180. doi:<https://doi.org/10.1016/j.cma.2024.117180>
532 URL <https://www.sciencedirect.com/science/article/pii/S0045782524004365>

533 [17] D. E. Burton, Connectivity structures and differencing techniques for staggered-grid
534 free-lagrange hydrodynamics, in: Seventh IMACS international conference on computer
535 methods for partial differential equations, International Association for Mathematics
536 and Computers in Simulation, IMACS Secretariat, New Brunswick, NJ, 1992, pp. 1–7.

537 [18] D. E. Burton, Consistent finite-volume discretization of hydrodynamic conservation
538 laws for unstructured grids, Tech. rep., Lawrence Livermore National Lab.(LLNL), Liv-
539 ermore, CA. United States. (1994).

540 [19] B. I. Bennett, J. D. Johnson, G. I. Kerley, G. T. Rood, Recent developments in the
541 sesame equation-of-state library, Tech. rep., Los Alamos National Lab. (LANL) (2 1978).
542 doi:10.2172/5150206.
543 URL <https://www.osti.gov/biblio/5150206>

544 [20] S. J. Bauer, B. Song, B. Sanborn, Dynamic compressive strength of rock salts, Interna-
545 tional Journal of Rock Mechanics and Mining Sciences 113 (2019) 112–120.

546 [21] K. Jha, D. Balakumar, R. Paluchamy, Experimental analysis of microstructure and
547 mechanical properties of copper and brass based alloys, International Journal of Auto-
548 motive & Mechanical Engineering 11 (2015) 2317–2331.

549 [22] D. Lazarus, The elastic constants of beta-brass, Physical Review 74 (11) (1948) 1726–
550 1727.

551 [23] E. R. Dobrovinskaya, L. A. Lytvynov, V. Pishchik, Properties of sapphire (2009) 55–
552 176doi:10.1007/978-0-387-85695-7 2.
553 URL <https://doi.org/10.1007/978-0-387-85695-7 2>

554 [24] H.-S. Kim, S. Roberts, Brittle–ductile transition and dislocation mobility in sapphire,
555 Journal of the American Ceramic Society 77 (12) (1994) 3099–3104.

556 [25] Z. Wang, A. Bovik, A universal image quality index, IEEE Signal Processing Letters
557 9 (3) (2002) 81–84. [doi:10.1109/97.995823](https://doi.org/10.1109/97.995823).

558 [26] S. C. Paulson, Z. A. Roberts, C. J. Sorensen, N. E. Kerschen, M. H. Harr, N. D. Parab,
559 T. Sun, K. Fezzaa, S. F. Son, W. W. Chen, Observation of damage during dynamic
560 compression of production and low-defect HMX crystals in Sylgard® binder using x-
561 ray phase contrast imaging, Journal of Dynamic Behavior of Materials 6 (1) (2020)
562 34–44. [doi:10.1007/s40870-019-00225-8](https://doi.org/10.1007/s40870-019-00225-8)
563 URL <https://link.springer.com/article/10.1007/s40870-019-00225-8>